

---

# SHREC 2021: CLASSIFICATION IN CRYO-ELECTRON TOMOGRAMS

---

\*Ilja Gubins<sup>1,2</sup>, Marten L. Chaillet<sup>2</sup>, Gijs van der Schot<sup>2</sup>, M. Cristina Trueba<sup>2</sup>, Remco C. Veltkamp<sup>‡</sup>, Friedrich Förster<sup>2</sup>, Xiao Wang<sup>3</sup>, Daisuke Kihara<sup>4,3</sup>, Emmanuel Moebel<sup>5</sup>, Nguyen P. Nguyen<sup>6</sup>, Tommi White<sup>7</sup>, Filiz Bunyak<sup>6</sup>, Giorgos Papoulias<sup>8</sup>, Stavros Gerolymatos<sup>8</sup>, Evangelia I. Zacharaki<sup>8</sup>, Konstantinos Moustakas<sup>8</sup>, Xiangrui Zeng<sup>9</sup>, Sinuo Liu<sup>9</sup>, Min Xu<sup>9</sup>, Yaoyu Wang<sup>10</sup>, Cheng Chen<sup>10</sup>, Xuefeng Cui<sup>10</sup>, Fa Zhang<sup>11</sup>

<sup>1</sup> Department of Information and Computing Sciences, Utrecht University, Netherlands

<sup>2</sup> Department of Chemistry, Utrecht University, Netherlands

<sup>3</sup> Department of Computer Science, Purdue University, USA

<sup>4</sup> Department of Biological Sciences, Purdue University, USA

<sup>5</sup> Inria Rennes Bretagne Atlantique, France

<sup>6</sup> Department of Electrical Engineering and Computer Science, University of Missouri, USA

<sup>7</sup> Department of Biochemistry & Electron Microscopy Core Facility, University of Missouri, USA

<sup>8</sup> Department of Electrical and Computer Engineering, University of Patras, Greece

<sup>9</sup> Computational Biology Department, Carnegie Mellon University, USA

<sup>10</sup> School of Computer Science and Technology, Shandong University, China

<sup>11</sup> Institute of Computing Technology, Chinese Academy of Sciences, China

## ABSTRACT

Cryo-electron tomography (cryo-ET) is an imaging technique that allows three-dimensional visualization of macro-molecular assemblies under near-native conditions. Cryo-ET comes with a number of challenges, mainly low signal-to-noise and inability to obtain images from all angles. Computational methods are key to analyze cryo-electron tomograms.

To promote innovation in computational methods, we generate a novel simulated dataset to benchmark different methods of localization and classification of biological macromolecules in tomograms. Our publicly available dataset contains ten tomographic reconstructions of simulated cell-like volumes. Each volume contains twelve different types of complexes, varying in size, function and structure.

In this paper, we have evaluated seven different methods of finding and classifying proteins. Seven research groups present results obtained with learning-based methods and trained on the simulated dataset, as well as a baseline template matching (TM), a traditional method widely used in cryo-ET research. We show that learning-based approaches can achieve notably better localization and classification performance than TM. We also experimentally confirm that there is a negative relationship between particle size and performance for all methods.

**Keywords** Cryo-electron tomography · Benchmark · Localization · Classification

## 1 Introduction

Cryo-electron tomography (cryo-ET) is an application of transmission electron microscopy, in which biological samples are cryogenically vitrified and imaged as they are sequentially tilted. The resulting “tilt-series” of 2D projections can be merged into a 3D reconstruction. Cryo-electron tomograms feature macromolecular assemblies in their cellular context, offering insight into life processes at its smallest scale Yahav et al. (2011). This data is key for improving our understanding and determining modes of actions of drugs.

---

\*For any questions, please contact by e-mail: [i.gubins@uu.nl](mailto:i.gubins@uu.nl)

†Conference version of the paper can be found here: <https://diglib.eg.org/handle/10.2312/3dor20211307>

The approach comes with a number of challenges. Imaging electrons strongly interact with biological matter, severely limiting the possible dose to avoid damaging the sample during imaging. The limited dose in turn limits signal-to-noise and effective resolution of the tomograms to about  $5nm$  (50). Such resolution is not enough to distinguish structural details of biomolecules. The common approach to increase resolution of the biomolecule of interest is subtomogram averaging Pfeffer and Mahamid (2018). It involves aligning and averaging copies of the same particles, introducing the challenge of correctly localizing and identifying those particles in the raw tomogram (Figure 1).

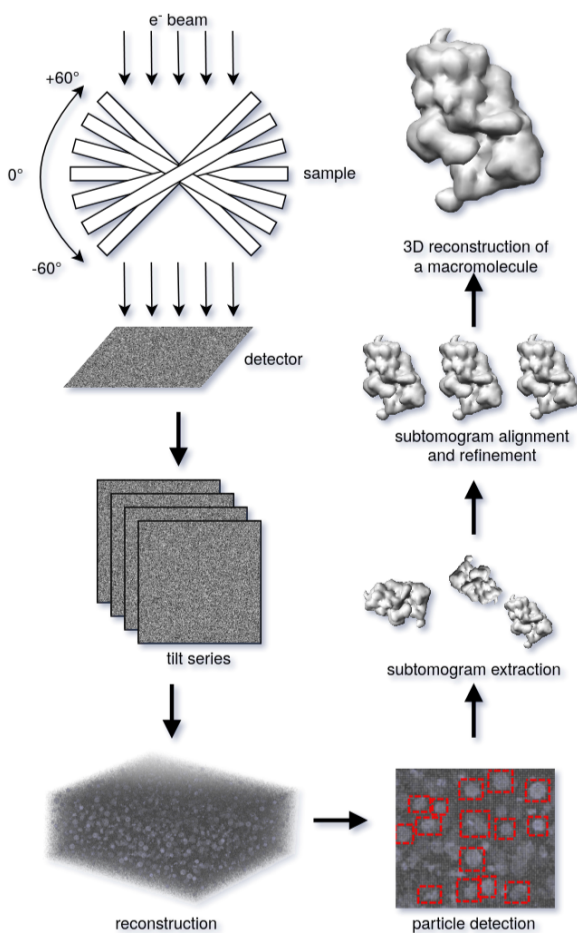


Figure 1: The overall process of cryo-electron tomography from data collection to reconstruction and subtomogram averaging.

detection of biomolecular structures in cryo-electron tomograms.

Our contributions are:

- We publish a new, publicly available, fully-annotated simulated cryo-electron tomography dataset. The dataset includes 12 protein classes, vesicles and gold fiducials.
- We evaluate and compare six learning-based methods and two versions of template matching.
- We note advantage of learning-based methods over template matching and show significant correlation between performance and molecular weight.

The remainder of this paper is organized as follows. Section 2 overviews dataset generation and benchmark evaluation. Then, in Section 3 we describe methods submitted for the evaluation. In Section 4 we present results. Finally, we discuss the results in Section 5.

Another major challenge is the constraint on imaging angles, up to  $\pm 60^\circ$  due to sample thickness, resulting in an incomplete reconstruction with a “missing wedge” in Fourier space. Manual analysis of such data is rarely feasible and often provides subjective results, leading to the interest in automated approaches. The most common of such approaches, for biological particles of known structures, is template matching Frangakis et al. (2002). Cross correlation between the template and the entire tomogram indicates locations and angles, where the template fits the best. For particles with unknown structures, reference-free methods must be used. The most common approach is based on applying Difference of Gaussian (DoG) Voss et al. (2009): a band-pass filter that removes noisy high frequency components and homogeneous low frequency areas, obtaining borders of the structures.

In recent years, machine learning has seen successful application to cryo-ET. Classical support vector machines have been used for both detection and classification Chen et al. (2012). With ever increasing amounts of data captured by cryo-EM and -ET methods Baldwin et al. (2018), deep learning methods are gaining popularity. Supervised methods were proposed for localization Wang et al. (2016), classification Che et al. (2018), end-to-end segmentation Chen et al. (2017a) and joint localization and classification Li et al. (2019), providing faster and often more accurate results than template matching Gubins et al. (2019). Moreover, methods based on clustering of representational features Xu et al. (2019), segmentation by manually designed rules Xu and Alber (2013) and geometric matching Zeng and Xu (2020) provide unsupervised and weakly-supervised alternatives, reducing the dependency on annotated data.

Each of the mentioned methods is validated on different tasks and different datasets (i.e., data acquisition parameters and microscopes), making it difficult to compare or draw conclusive results about their relative performance. With this benchmark, we aim to support researchers involved in developing new methods for localization and

PDB	Name	Mol. weight ( <i>kDa</i> )	Volume ( <i>nm</i> <sup>3</sup> )	Area ( <i>nm</i> <sup>2</sup> )	Sphericity	Eff. radius ( <i>nm</i> )
1s3x	Hsp70 ATPase	42.75	90.82	109.8	0.89	2.481
3qm1	LJ0536 S106A	62.62	127.9	137.6	0.892	2.789
3gl1	Ssb1, Hsp70	84.61	196.5	191.2	0.855	3.083
3h84	GET3	158.08	347	370.9	0.644	2.807
2cg9	Hsp90-Sba1	188.73	401.2	358.4	0.734	3.358
3d2f	Sse1p, Hsp70	236.11	516	459.6	0.677	3.368
1u6g	Cand1-Cul1-Roc1	238.82	499.3	450.2	0.676	3.327
3cf3	P97/vcp	541.74	1136	745.2	0.707	4.573
1bxn	Rubisco	559.96	1021	583.4	0.84	5.25
1qvr	ClpB	593.36	1354	1063	0.557	3.821
4cr2	26S proteasome	1309.28	2675	1846	0.505	4.347
5mrc	Yeast mito ribosome	3325.59	6372	3161	0.526	6.047

Table 1: Macromolecular complexes present in the dataset, sorted by their molecular weight. Volume, area, sphericity and effective radius are computed from particle volumes with threshold density  $> 0.5$ .

## 2 Benchmark

We propose a task of localization and classification of particles in the cryo-electron tomogram volume. A benchmark is conducted on a simulated cryo-electron tomogram populated with randomly positioned and oriented copies of structurally well-defined molecular complexes. In total, the volume contained 1,571 particles of 13 different classes. To facilitate application of learning-based methods, we also provide nine tomograms with similar protein distribution and ground truth data that was used for the simulation.

### 2.1 Dataset

First, we select 12 proteins of known structure of varying size, shape and functions (Table 1). To characterize them, we calculate sphericity,  $\Psi$ , a measure of how much the volume resembles a sphere:

$$\Psi = \frac{\pi^{1/3} \times (6V)^{2/3}}{A} \quad (1)$$

and effective radius, the radius of a sphere with the same surface area to volume ratio as the volume of interest:

$$r_{eff} = \frac{3V}{A} \quad (2)$$

where  $V$  is the volume and  $A$  is the surface area.

For all molecules placed in the simulation, we first calculated an interaction potential. We define this potential as a sum with a real and imaginary part  $V_{int} = V_{el} + iV_{ab}$ . The electrostatic potential  $V_{el}$  determines the elastic scattering of each molecule which influences phase contrast. We calculated it by placing on each atom’s center a sum of 5 Gaussians that are parameterized by atom specific scattering factors Rullgård et al. (2011). We extended this electrostatic potential calculation scheme by correcting each atom for solvent exclusion Fraser et al. (1978). This was modelled by subtracting a smooth spherical volume around each atom with a Van der Waals radius determined by atom type, and an amorphous ice background potential of  $4.530V$ . The second part of the potential - the absorption potential  $V_{ab}$  - is dependent on molecule-type (i.e. protein, membrane, gold, or amorphous ice), and gives rise to absorption contrast through inelastic scattering Vulović et al. (2013).

We generated interaction potential maps of proteins, vesicles and gold fiducials at 5. Then, without overlaps, we place 1,000 to 3,000 proteins, 7 to 14 gold fiducials and 2 to 7 vesicles at random locations and in random  $SO(3)$  orientations, into the ground truth “grandmodel” - the box containing ground truth of the sample simulation. For each placed particle we save class, center coordinates and Euler angles in  $ZXZ$  notation. That allows us to generate class masks (voxel to class mapping) and occupancy masks (voxel to particle mapping).

To simulate the embedding ice layer of the grandmodel, we added background constants of amorphous ice to the interaction potential of the grandmodel (corresponding to  $4.530V$  for the elastic part and 0.208 inelastic scattering fraction). These constants were both calculated assuming an amorphous ice density of  $0.93g/cm^3$ , and for the

absorption constant a  $300kV$  electron beam. Each grandmodel was rotated over 61 evenly spaced tilt angles ranging from  $-60^\circ$  to  $+60^\circ$ , with cubic b-spline interpolation Ruijters and Thévenaz (2012) to minimize rotation artifacts.

To calculate the projection image for each rotation angle we implemented the multislice method Vulović et al. (2013). This method models the defocus gradient through the ice layer by propagating the electron wave through slices of the model. We set the size of these slices to  $5nm$ . After calculating the wave propagation through the sample we obtain the exit wave in the image plane. To get the final projection image we multiplied the exit wave by the microscope’s contrast transfer function (CTF) and envelope functions using a defocus of  $3.5\mu m$  on average (see below), an acceleration voltage of  $300kV$ , spherical aberration of  $2.7mm$ , a source energy spread of  $0.7eV$ , an illumination aperture of  $30/mum$ , and objective diameter of  $100/mum$ , a focal distance of  $4.7mm$ , and no astigmatism. For the detection process we then convoluted the exit wave with the DQE of the K2SUMMIT detector. For the final electron counts, we sampled from the Poisson distribution, with an electron dose of approximately  $1.6 e^-/\text{\AA}^2$ . The final images were  $1024 \times 1024$  pixels with a pixel size of 5. We did a weighted back-projection reconstruction while binning the projections 2 times to obtain the final tomograms of  $512 \times 512 \times 512$  with a sampling of  $1nm/voxel$ . This means the initial models are oversampled compared to the final reconstruction, improving accuracy for the sample-microscope interaction.

To introduce variation between tomograms we randomly selected a defocus between 2 and  $5\mu m$  for each model, and an electron dose between 100 and  $120 e^-/\text{\AA}^2$  for the full tilt range (which was equally divided over the 60 tilt images). We set random shifts for each projections in a  $1nm$  range in the  $x$  and  $y$  direction, to introduce misalignment of the projections and deteriorate reconstruction quality. This resulted in the tomograms varying in final SNR from 0.12 to 0.58 (the evaluation model 0.24), as calculated with  $SNR = \sigma_{signal}^2 / \sigma_{noise}^2$ , where  $\sigma_{signal}^2 = \sigma_{noisysignal}^2 - \sigma_{noise}^2$  (where the considered signal comes from all classes, including gold markers).

We noticed that in the power spectra (representing the amplitudes of the Fourier transform) of simulated projections, Thon rings were difficult to see. These are usually pronounced in experimental images (compared with data recorded at similar conditions; mixedCTEM from EMPIAR-10064). By scaling the amplitudes in Fourier space with amplitudes from experimental images (mixedCTEM) we qualitatively improved the appearance and made the simulation more similar to experimental images. We implemented this in a similar fashion to Fourier ring correlation (FRC), where for each ring of the Fourier amplitudes of the simulated image, we scaled the values to the mean of that same ring from an experimental image:  $A_{scaled} = \sum_i^N M_i A_{sim}(\mu_i^{exp} / \mu_i^{sim})$ , where  $N$  is the number of rings,  $M$  is the bandpass mask, and  $\mu$  the mean of a band. We then obtained the updated simulated image by recombining the scaled amplitudes with the phase information of that image in Fourier space.

## 2.2 Evaluation

The main goal of the benchmark is to localize and classify biological particles in the tomographic reconstructions. The performance of the submissions has been evaluated solely on the test tomogram, the only tomogram for which ground truth is not available.

During evaluation, we parsed the submitted result and computed some commonly adopted performance metrics for classification and localization. The metrics are precision (Equation 3): percentage of results which are relevant; recall (Equation 4): percentage of total relevant results correctly classified; F1 score (Equation 5): harmonic average of the precision and recall; false negative rate also known as miss rate (Equation 6): percentage of results which yield negative test outcomes. We also record how far the predicted center was from the ground truth center and how many results refer to the same particles.

$$\text{Precision} = \frac{\text{true positive}}{\text{true positive} + \text{false positive}} \quad (3)$$

$$\text{Recall} = \frac{\text{true positive}}{\text{true positive} + \text{false negative}} \quad (4)$$

$$\text{F}_1 \text{ score} = 2 \cdot \frac{\text{precision} \cdot \text{recall}}{\text{precision} + \text{recall}} \quad (5)$$

$$\text{Miss rate} = 1 - \text{recall} \quad (6)$$

### 2.2.1 Erratum

During evaluation stage of the benchmark we have discovered an error in the dataset. One of the classes, protein 4v94, has been generated incorrectly and always appeared twice next to each other. Moreover, the center of such doubled-particle was in the empty space between them. The reason is that the PDB upload was a mirrored structure, while naturally the protein occurs as a single particle. While that does not present a problem for semantic segmentation approaches that are trained on class masks, it is a problem for approaches that use the center locations that we provide. For the fairness of benchmark we have decided to remove 4v94 protein from the evaluation completely. After the competition has finished, we have fixed reported center locations in the updated version of the dataset.

### 2.3 Comparison with earlier benchmarks

Localization and classification of particles in cryo-ET is an open problem with major challenges due to the nature of imaging process and biological sample size. Previous editions of this benchmark Gubins et al. (2019, 2020) already provide some insight into automated localization and classification methods for cryo-ET. In this edition, we significantly improved dataset generation process (Section 2.1: multislice method, varied defocus and electron dose, Fourier scaling to experimental images) and introduced membranes as an additional semantic class.

## 3 Participants and methods

Nine international research groups registered to the track, of which seven submitted their results. Each participant could submit as many result sets as long as they present an interesting difference, e.g. different selection of hyperparameters for the same method. In total, the benchmark compares eight result sets obtained with seven different methods listed in this section.

### 3.1 URFinder: Macromolecules localization using combined 3D UNet3+ and ResNet

By: Xiao Wang, Daisuke Kihara

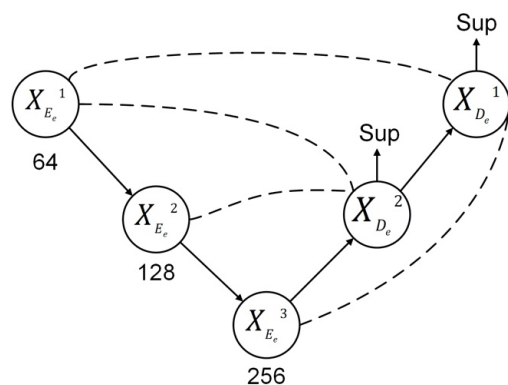


Figure 2: The architecture of 3D UNet3+.

The method named URFinder is based on deep learning techniques, 3D UNet3+ Huang et al. (2020) and 3D ResNet He et al. (2016a); Hara et al. (2017) for 3D semantic segmentation of the tomogram data. 3D UNet3+ was used to detect 13 protein types. 3D ResNet was used for two classifications, one for detecting 13 protein types and the other for detecting gold fiducials. For protein detection, results of 3D UNet3+ and 3D ResNet were combined.

Given a voxel (a cropped 3D region) from a tomogram, the proposed 3D-UNet3+ takes the voxel as input and outputs the 14 probability scores, for 13 proteins and background, for each grid point in the voxel. The size of each 3D input slice was set to  $64 \times 64 \times 64$  and the stride size was set to 16 to scan the whole cryo-ET map. We extended the original UNet3+, which was developed for 2D image, to 3D. In our architecture we have 2 down-sampling and 2 up-sampling operations instead of 4 in the original UNet3+. The architecture of our 3D UNet3+ is shown in Figure 2. All other configurations, such as convolution and maxpooling filter sizes, the number of filters and the stride size, are the same as UNet3+.

Two networks with 3D ResNet were trained. One is for protein detection, which is 14 class (13 proteins and background) multi-class classification, and the other for binary classification for gold fiducials. 3D ResNet had 20 layers Huang et al. (2020); He et al. (2016a) and the size of each 3D input slice was set to  $32 \times 32 \times 32$ .

We used tomograms 0 to 7 for training and validation while the tomogram 8 was kept for testing. For UNet3+ training, we scanned the whole map with a stride of 16 with a voxel of  $64 \times 64 \times 64$ . We adopted the deep supervision technique in Zhou et al. (2018). For output of each decoder, the binary cross-entropy (BCE) loss was applied and the total loss was defined as the sum of the individual losses. We used the Adam optimizer Kingma and Ba (2014) with an initial learning rate 0.0001 and a weight decay of  $1e^{-4}$ . The cosine learning rate scheduler Loshchilov and Hutter (2016) was used to decay the learning rate to  $1e^{-5}$ . For 3D ResNet training, we first sampled negative (background) examples from the provided training tomograms by extracting voxels with the center that is not closer than 16 grid units to any proteins

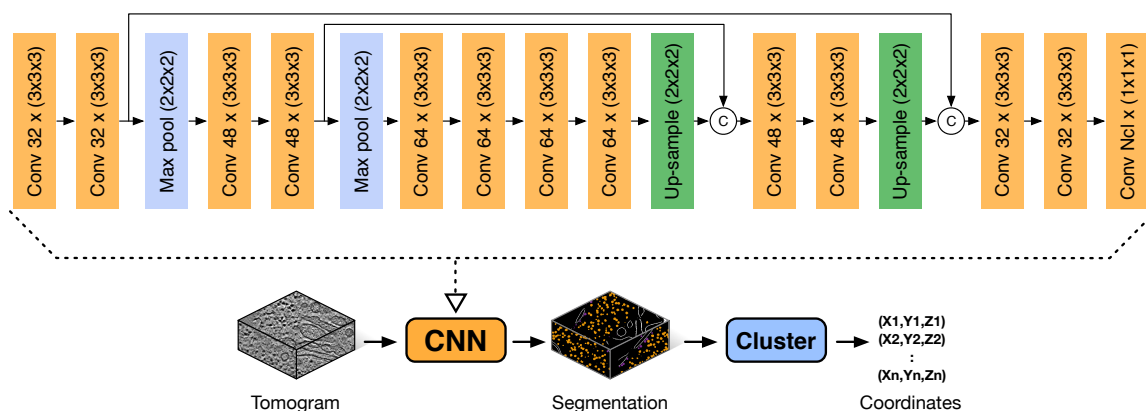


Figure 3: Top: CNN architecture used in DeepFinder. All convolutional layers are followed by a ReLU activation function, except the last layer which uses a soft-max function. The up-sampling is achieved with up-convolutions (also called “backward-convolution”). Combining feature maps from different scales is performed by concatenation along channel dimension.

Bottom: workflow depicting how macromolecule coordinates are obtained from the segmentations generated by the CNN. A clustering algorithm (mean-shift) is applied on the segmentation map to differentiate individual macromolecules.

and gold fiducials. For each positive voxel that have a protein or a gold fiducial at the center, we augmented them by random flips and rotations. We had in total 620, 892 voxels for multi classification for detecting proteins. We had in total 2160 positive voxels and 43916 negative voxels for binary classification. In the training process, we used the Adam optimizer with learning rate of 0.002 and a weight decay of  $1e^{-4}$ . In total, we train the network for 30 epochs.

In the inference stage, we applied three networks, 3D UNet3+, 3D ResNet for protein detection and another ResNet for gold fiducial detection. 3D UNet3+ scanned the whole cryo-ET map with a stride of 16 to extract  $64 \times 64 \times 64$  voxels and made predictions at each grid point in the voxels. If a grid point has multiple assignments from different voxels, we used the average probabilities as the final predictions. We removed connected components with less than 64 voxels and used centers of the rest for the reported protein particles. For 3D ResNet, we used a voxel of  $32 \times 32 \times 32$  and a stride of 2 to scan the whole map and made predictions to the center of the voxel. When detecting proteins, we checked the connected components and filtered out those components with less than 64 voxels. For binary gold fiducial detection, too large components with width, height or length larger than 40 voxels and too small components with less than 27 voxels were removed. Finally, detected proteins by 3D UNet3+ and 3D ResNet were combined. If detected proteins by the two methods overlap or locate in direct neighboring voxels they were merged into one protein. The center of connected components were reported as the location of detected proteins and gold fiducials.

All the experiments were performed on NVIDIA Quadro RTX 8000 GPU. For 3D UNet3+, the training time was 7 days for 30 epochs on 2 RTX 8000 GPU. The production time including inference and filtering was 72 minutes on 1 RTX 8000 GPU. For 3D ResNet, the training time was 4 days for the multi-class and 1.5 days for binary classification of gold fiducials for 30 epochs on 1 RTX 8000 GPU, and the production time was 54 minutes including the inference and filtering.

### 3.2 DeepFinder: Deep learning improves macromolecules localization and identification in 3D cellular cryo-electron tomograms

By: Emmanuel Moebel

DeepFinder Moebel et al. (2020) is a computational tool for multiple macromolecular species localization, based on supervised deep learning. This two-step procedure (Figure 3) first produces a segmentation map where a class label is assigned to each voxel. The classes can represent different molecular species (e.g. ribosomes, ATPase), states of a molecular species (e.g. binding states, functional states) or cellular structures (e.g. membranes, microtubules). In the second step, the segmentation map is used to extract the positions of macromolecules. To perform image segmentation, we use a 3D CNN whose architecture and training procedure have been adapted for large datasets with unbalanced classes. The analysis of the obtained segmentation maps (Figure 4) is achieved by clustering the voxels with the same label class, using the mean-shift algorithm with different radii (bandwidth) for each class. Hence, the detected clusters correspond to individual macromolecules and their positions can then be derived.

The 3D CNN architecture is trained with Adam Kingma and Ba (2014) optimizer, using 0.0001 as learning rate, 0.9 as exponential decay rate for the first moment estimate and 0.999 for the second moment estimate. A Dice loss Sudre et al. (2017) is used to estimate the network parameters. The training took 50 hours on an Nvidia M40 GPU. For large and medium macromolecules, presented scores are reached after 22 hours; the additional time is necessary for having better performance with small macromolecules. The segmentation and clustering of a  $512 \times 512 \times 200$  tomogram takes 20 minutes.

With feasibility in mind, we developed training strategies to assist the user in producing segmentation maps (needed for training the CNN) from tomogram annotations consisting of the spatial coordinates of macromolecules. DeepFinder is an open-source python package with a graphical interface aimed towards non-computer scientist users.

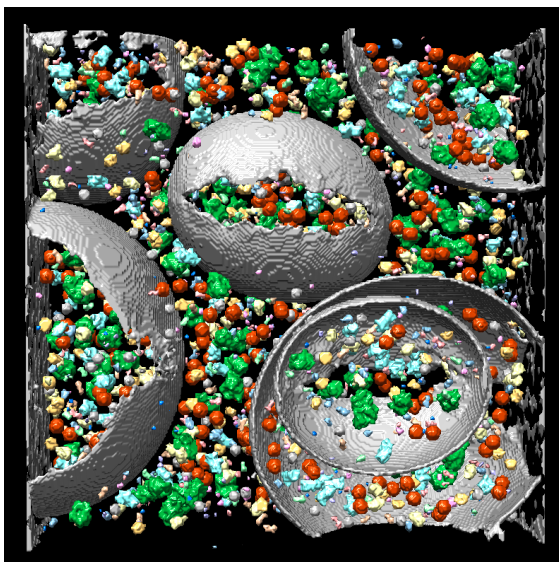


Figure 4: Test tomogram segmentation with DeepFinder method.

### 3.3 U-CLSTM: U-net architecture with convolutional long short term memory decoder

**By:** Nguyen P. Nguyen, Tommi A. White, Filiz Bunyak

To predict particle location, we employed the U-net architecture Ronneberger et al. (2015) network. Our network's encoder has three main layers, each layer contains 20 residual blocks Zhang et al. (2017). It's not necessary for both the encoder and decoder to have the same configuration. We wanted to make use of the context memory mechanism Milletari et al. (2018) by using a convolutional long short term memory (CLSTM) cell Shi et al. (2015) in the decoder. This decoder architecture can exploit all image features from coarse to fine levels, further refine location prediction. The encoder and decoder are connected by the atrous spatial pyramid pooling block Chen et al. (2017b). Instead of using mask segmentation to obtain particle centers, we applied regression to predict a heatmap of particle locations as in Nguyen et al. (2021). Each heatmap contains 15 channels, corresponding to 15 types of particles to be detected. Different image volumes have different noise levels and different distributions of particles. We employed weighted sampling to balance the occurrence of data samples, and the small particles also have higher sampling weights. The ground truth heatmap was generated from a binary ground truth masks using distance transform. We then used a mean squared error loss function to optimize the network parameters. U-CLSTM was trained with patches of size  $96 \times 96 \times 96$  on an NVIDIA Quadro RTX-5000 GPU in 120 hours. Total prediction time is 15 minutes for each image volume  $512 \times 512 \times 512$ , which includes both heatmap prediction time and particle center detection time. Thresholding and connected component labeling were applied to each channel of the predicted heatmap to localize and segment the particle centers. Spurious detections were filtered out based on detection size. Particles whose centroids are located within 5 voxels from the ground truth particle centroids in terms of Euclidean distance are considered as detected. Detections who predict the same particle type as the corresponding ground truth particle, are considered as correct classification.

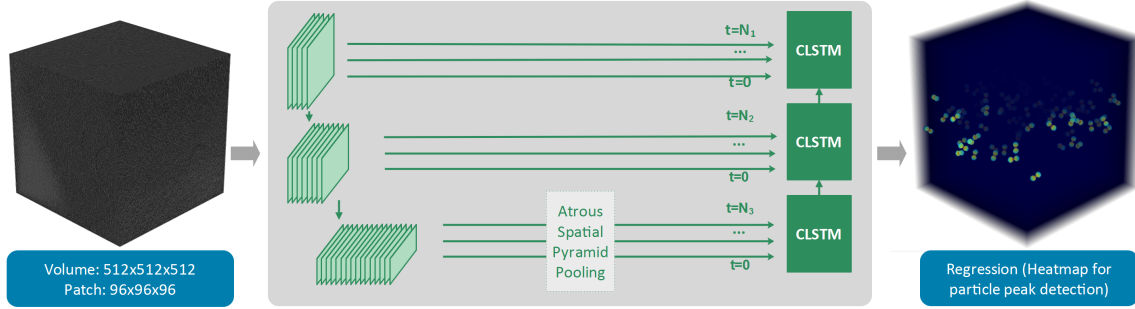


Figure 5: U-CLSTM: U-net architecture with convolutional long short term memory (CLSTM) decoder

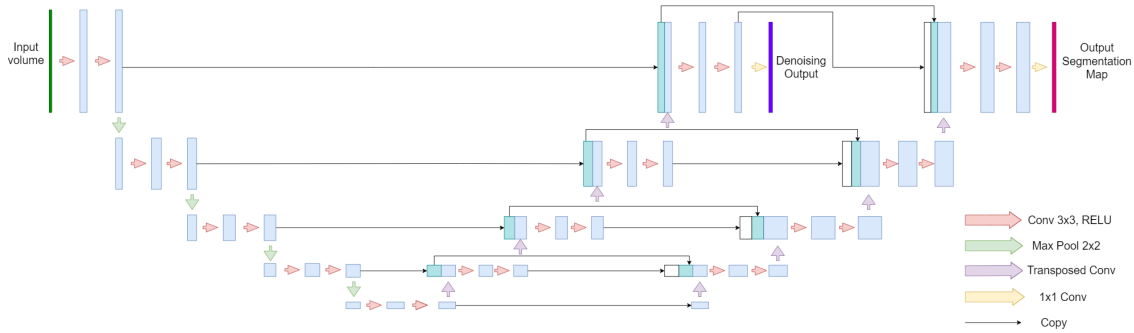


Figure 6: Topology of Multi-Cascade DS Network

### 3.4 Multi-Cascade DS Network

**By:** Giorgos Papoulias, Stavros Gerolymatos, Evangelia I. Zacharaki, Konstantinos Moustakas

We formulated the classification and localization tasks as a supervised (volumetric) segmentation and morphological analysis problems, respectively. We solved the segmentation task jointly with denoising by employing a deep encoder-decoder architecture inspired by the cascaded network in Gubins and Veltkamp (2020). Specifically, we implemented a multi-cascade DS (Denoising-Segmentation) network based on the popular 3D U-Net Ronneberger et al. (2015) and composed of two decoding pathways. The two pathways perform denoising on the input data (3D tomogram) and volumetric segmentation (to produce a 3D label map), respectively. The whole architecture is illustrated in Figure 6.

In more details, in the denoising output pathway each decoder block is connected to the respective encoder layer with a skip connection, while in the segmentation output pathway each block receives the skip connections from the respective layers of both the encoding pathway and the denoising decoding pathway. The connectivity introduced between decoding pathways is considered to facilitate inductive transfer between early and later stages of a deep cascade. Thus, this approach is more suitable than architectures dealing with denoising and segmentation in a serial fashion. Additionally, it is less computationally expensive as a serialized architecture would practically require the training of two deep networks, one for each learning task, independently.

We set the depth of the employed deep network to 5 and the number of filters to 16, 32, 64, 128 and 256 in the respective layers, yielding 13.57 M of parameters in total. For the denoising task, we use the RMSE loss between the reconstruction and the respective grandmodel volumes and for 3D segmentation, we employ the Tversky loss function with  $\alpha = 0.7$  and  $\beta = 0.3$  using the ground truth segmentation masks as target. The unified loss function minimized during optimization includes the sum of the previous two loss terms. Loss minimization is performed using the Adam optimizer Kingma and Ba (2014) using an initial 0.001 learning rate explicitly defined by a Cosine Annealing learning rate scheduler. The model was trained for 20 epochs using a batch size of 20 on an NVIDIA GeForce RTX 3090 graphics card. PyTorch with CUDA acceleration was utilized for the implementation. Finally, the training procedure lasted 22 hours and the inference time was approximately 5 min.

Regarding the given dataset exploitation, the tomograms were cropped into cubic volumes (also denoted as subtomograms) with a size of  $64^3$  using a 75% overlap in all three dimensions. Half of the generated cubic volumes were



horizontally and vertically flipped randomly during the training procedure for data augmentation purposes. Subtomograms from tomograms 0 to 7 were used for training and subtomograms from tomogram 8 for validation and optimization of hyper-parameters.

After having derived the 3D segmentation maps, connected component analysis (with neighborhood 26) is performed to identify the individual particles as uniform clusters, followed by two post-processing steps. First, spurious clusters that consist of less than 5 voxels are removed and then classes are merged inside each component by assigning the most frequently occurring label to the whole component. Finally, the centroids of each component are estimated as the center of mass to address the localization challenge.

### 3.5 YOPO: one-step object detection for cryo-ET macromolecule localization and classification

By: Xiangrui Zeng, Sinuo Liu, Min Xu

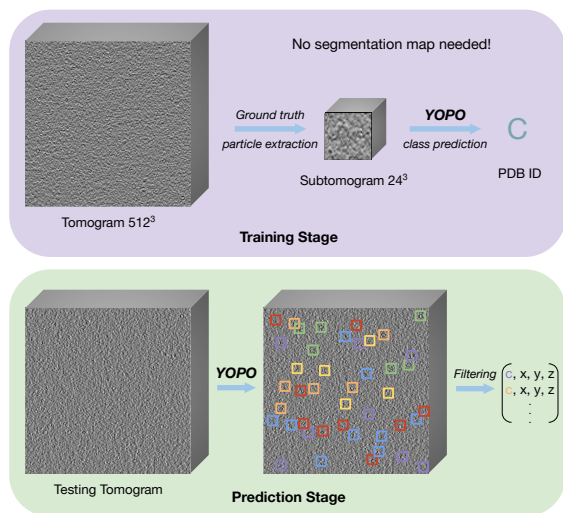


Figure 7: YOPO: Flowchart of macromolecule detection.

We formulate a novel one-step object detection framework specifically designed for cryo-ET data (Fig. 7). Previous deep learning-based works on detecting particles in cryo-electron tomograms are either two-step classification (extract potential structural regions as subtomograms and then perform classification) or segmentation methods. Considering two important properties of subtomogram data: (1) the high-level structural details of a particle determine its function and identity and (2) the particle is of random orientation and displacement inside a subtomogram, we designed a convolutional neural network named YOPO Zeng et al. (2021), which retains discriminative high-level structural details and achieve the maximal transformation-invariance. The flowchart of macromolecule localization and classification using YOPO is illustrated in Fig. 7.

In the training stage, only particle location ground truth was used to train the YOPO network to predict the PDB ID of a subtomogram. In the testing stage, the trained YOPO network was applied on the tomogram level to directly predict both the location and PDB ID of detected macromolecules. From each training tomogram, we extract subtomograms of size  $32^3$  according to the ground truth particle location file. An additional 20,000 subtomograms were extracted at random locations from the background. Therefore, there are  $K = 15$  classes in total

including the background class and excluding vesicle centers. Subtomograms from tomogram 0 to 7 were used as training data and subtomograms from tomogram 8 as validation data. The training took 8 hours on one NVIDIA GeForce Titan X GPU. The trained model predicted at every location by applying the learned model parameters on the whole testing tomogram. Locations with high confidence (probability  $> 0.9$ ) to be one of the structural classes were kept. We then filtered the locations to ensure that the minimum distance between two detections was greater than 14 voxels. As a one-step object detection method, the classification and localization tasks are unified in an end-to-end fashion.

YOPO is an efficient cryo-ET macromolecule detection (localization + detection) framework in two aspects: (1) the only ground truth information used for training is the particle locations and classes in ground truth particle location file; (2) YOPO performs prediction on the subtomogram level at every location, which is similar to the traditional template matching approach. However, the whole prediction on one tomogram took only about 40 min using one GPU instance.

### 3.6 Central Feature Network (CFN) for cryo-EM particle classification and localization

By: Yaoyu Wang, Cheng Chen, Fa Zhang, Xuefeng Cui

We introduced a novel Central Feature Network (CFN) for the general 3D object detection problem, and applied it on the Cryo-EM particle detection problem. Specifically, CFN takes  $64 \times 64 \times 64$  sub-tomograms as input, and detects particles in the input sub-tomograms. As shown in Figure 1a, CFN is based on a 3D ResNet model He et al. (2016a,b) with dilated convolutions Yu and Koltun (2015) and the focal loss function Lin et al. (2017). Notably, our CFN model

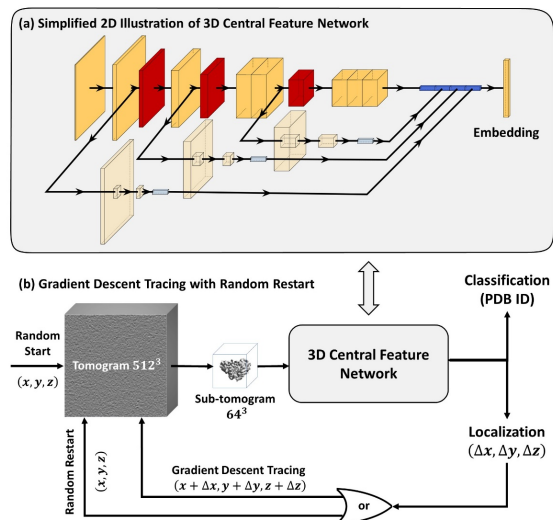


Figure 8: Central Feature Network (CFN) architecture and inference pipeline

is different from existing models with three novel modifications. First, existing methods use only the neurons of the last convolutional block for predictions, while we combine the central neurons (i.e., blue boxes in Figure 8a) of each convolutional block for predictions. This helps to identify particles with different sizes because deeper networks are more suitable for bigger particles while shallower networks are more suitable for smaller particles. Second, existing methods use average pooling (or max pooling) for dimension reduction, while we use bottlenecked pooling (i.e., red boxes in Figure 8a) with two fully connected layers for the same task. By avoiding location irrelevant operations (e.g., average or max), location information could be retained from layers to layers. Finally, existing methods focus on only classifications, while we perform both classifications and localizations at the same time.

As shown in Figure 8b, the localization results of CFN can be used to trace the particle centers via a gradient decent approach with a random restart. Specifically, an initial sub-tomogram is randomly sampled, and CFN is used to detect the particle in the sub-tomogram. If a particle is detected, the predicted particle center is used to sample another sub-tomogram. This center tracing process is repeated with a random restart so that all sub-tomograms can be sampled theoretically, while the sub-tomograms near particle centers are more likely to be sampled. Finally, near-center predictions are clustered to produce a consensus prediction. The training and testing process took four days on two NVIDIA 3090 video cards.

### 3.7 Template matching

**By:** M. Cristina Trueba, Marten L. Chaillet

We performed template matching on the simulated dataset using the cryo-ET analysis framework PyTom Hrabe et al. (2012). A solvent corrected electrostatic potential sampled to a grid of 1 nm voxels was modulated for each particle with a CTF curve at 3,65  $\mu m$  defocus in the frequency domain to serve as templates Fraser et al. (1978). The templates were flipped to cover left- and right-handedness in the particle orientation of the simulated dataset. In addition, a Gaussian low pass filter set to 4 nm was applied in Fourier space to both the template and the tomogram to increase contrast and facilitate the particle detection. Spherical template masks with Gaussian smoothed edges were used for normalization of the cross-correlation value. The masks radius for each particle was chosen to fully encompass the template. We also used Laplace of Gaussian (LoG) with standard deviation ( $\sigma$ ) of 5 to recognize gold markers and extract their position. Template matching for 12 protein classes and both handedness takes 4 hours and 26 minutes on the NVIDIA GeForce GTX 1080 Ti (20 min 40 s per class, 10 min 20 s per handedness).

**TM.** The top 1,000 candidates with the highest cross-correlation score for each class were extracted and merged for the different particle handedness. A Gaussian distribution was fitted to the histogram of the correlation scores for each case pursuing to identify the correct particle population in it. We objectively set a minimum threshold to the mean ( $\mu$ ) minus two times the standard deviation ( $\sigma$ ) of the fitted gaussian population to avoid false positives. This resulted

in 9 fiducials and 122, 107, 318, 314, 924, 708, 211, 329, 127, 399, 149, 301 particles of each class in the gold marker excluded dataset, from largest to smallest with a total of 4,009 particles recognized.

**TM-F.** Alternatively, candidates of each class were additionally filtered to exclude those that would potentially be overlapped with already selected particles. To test for overlap, we calculate the distance between the centre of an existing particle to the centre of the candidate and calculate whether the distance is smaller than the sum of their radii. The candidates for round and symmetrical particles were filtered before asymmetrical and elongated particles as their performance was significantly better based on visual inspection in PyTom. This resulted in 9 fiducials and 122, 81, 79, 127, 624, 212, 37, 71, 125, 85, 32, 65 particles of each class recognized in the gold marker excluded dataset, from largest to smallest respectively with a total of 1,660 particles selected.

## 4 Results

We have evaluated different metrics (Section 2.2) that allows comparison of localization (Table 3) and classification (Table 4) performance of the methods. For more convenient referencing, we have assigned following short names to the methods:

1. URFinder (Section 3.1)
2. DeepFinder (Section 3.2)
3. U-CLSTM (Section 3.3)
4. MC DS Net (Section 3.4)
5. YOPO (Section 3.5)
6. CFN (Section 3.6)
7. TM-T and TM-F (Section 3.7)

The test tomogram has 1,571 particles of the same 13 classes and same distribution as the training data (Table 2). To have a more detailed classification evaluation, we compare results with cumulative F1 score (Figure 9), as well as group proteins by their molecular weight (Table 5) and average F1 scores for an additional metric correlated with particle sizes (Table 6).

Particle	Quantity
1s3x	122
3qm1	120
3g11	123
3h84	144
2cg9	125
3d2f	140
1u6g	143
3cf3	139
1bxn	135
1qvr	127
4cr2	115
5mrc	121
fiducial	11

Table 2: Distribution of particles by class in the test tomogram.

## 5 Discussion

The benchmark allowed us to compare baseline template matching and upcoming learning-based methods, as well as highlight current challenges and approaches in cryo-ET.

### Learning-based vs. template matching

The results (Table 3, 4) show that all learning-based methods achieve better scores than the traditional baseline template matching (TM). Learning-based methods are also at least twice faster (Table 7) than optimized GPU-accelerated TM,

Method	RR	TP	FP	FN	MH	AD	Recall	Precision	Miss rate	F1
URFinder	1969	1298	377	267	149	1.84	0.826	0.659	0.174	0.733
DeepFinder	1567	1362	64	203	20	2.22	0.867	<b>0.869</b>	0.133	<b>0.868</b>
U-CLSTM	1460	1253	<b>49</b>	312	44	2.13	0.798	0.858	0.202	0.827
MC DS Net	1760	<b>1415</b>	239	<b>150</b>	56	1.59	<b>0.901</b>	0.804	<b>0.099</b>	0.850
YOPO	1627	1224	232	341	<b>14</b>	1.66	0.720	0.752	0.221	0.765
CFN	1765	1364	239	201	20	<b>1.52</b>	0.868	0.773	0.132	0.818
TM-F	1772	963	295	601	17	2.65	0.613	0.543	0.387	0.576
TM	4195	1073	583	492	716	2.62	0.683	0.256	0.317	0.372

Table 3: Results of localization evaluation. *RR*: results reported; *TP*: true positive, unique particles found; *FP*: false positive, reported non-existent particles; *FN*: false negative, unique particles not found; *MH*: multiple hits: unique particles that had more than one result; *AD*: average euclidean distance from predicted particle center in voxels; *Recall*: uniquely selected true locations divided by actual number of particles in the test tomogram; *Precision*: uniquely selected true locations divided by RR; *Miss rate*: percentage of results which yield negative results; *F1 Score*: harmonic average of the precision and recall. The best results in each column are highlighted.

Method	1s3x	3qm1	3gl1	3h84	2cg9	3d2f	1u6g	3cf3	1bxn	1qvr	4cr2	5mrc	fiducial
URFinder	0.000	0.423	0.453	0.600	0.542	0.672	0.673	0.867	0.967	0.860	0.926	0.954	0.429
DeepFinder	<b>0.402</b>	0.481	0.517	0.701	0.716	0.766	0.737	0.964	0.989	0.953	0.974	0.996	<b>1.000</b>
U-CLSTM	0.277	0.415	0.389	0.561	0.511	0.651	0.566	0.946	0.989	0.903	0.991	<b>1.000</b>	<b>1.000</b>
MC DS Net	0.316	0.487	0.603	<b>0.783</b>	<b>0.782</b>	<b>0.791</b>	<b>0.797</b>	0.956	0.985	0.934	0.979	<b>1.000</b>	<b>1.000</b>
YOPO	0.203	0.148	0.471	0.601	0.626	0.627	0.613	0.884	0.938	0.920	0.983	0.966	0.952
CFN	0.250	<b>0.511</b>	<b>0.613</b>	0.768	0.714	0.761	0.731	<b>0.971</b>	<b>0.996</b>	<b>0.969</b>	<b>0.996</b>	<b>1.000</b>	<b>1.000</b>
TM-F	0.040	0.189	0.200	0.282	0.308	0.439	0.129	0.592	0.962	0.513	0.827	0.857	0.900
TM	0.054	0.197	0.266	0.302	0.345	0.452	0.133	0.615	0.966	0.545	0.950	0.857	0.900

Table 4: Results of classification evaluation for all classes. The values correspond to F1 score achieved by methods on specific classes. The best results in each column are highlighted.

Group	Weight	Proteins
Small	<200	1s3x, 3qm1, 3gl1, 3h84, 2cg9
Medium	200-600	3d2f, 1u6g, 3cf3, 1bxn, 1qvr
Large	600+	4cr2, 5mrc

Table 5: Grouping of macromolecular complexes by their molecular weight in *kDa*

Method	Small	Medium	Large
URFinder	0.404	0.808	0.94
DeepFinder	0.563	0.882	0.985
U-CLSTM	0.431	0.811	0.996
MC DS Net	<b>0.594</b>	<b>0.893</b>	0.989
YOPO	0.41	0.796	0.974
CFN	0.571	0.886	<b>0.998</b>
TM-F	0.204	0.527	0.842
TM	0.233	0.542	0.903

Table 6: F1 scores of each submission for size group defined in Table 5. The best results in each column are highlighted.

Method	Training stage	Inference stage
URFinder	300h	2h 6m
DeepFinder	50h	20m
U-CLSTM	120h	15m
MC DS Net	22h	5m
YOPO	8h	40m
CFN		96h
TM-F/TM GPU	N/A	4h 26m

Table 7: Reported training and inference stages timings.

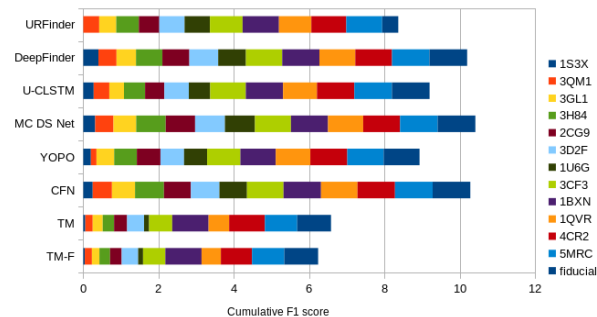


Figure 9: Cumulative classification F1 scores of methods.

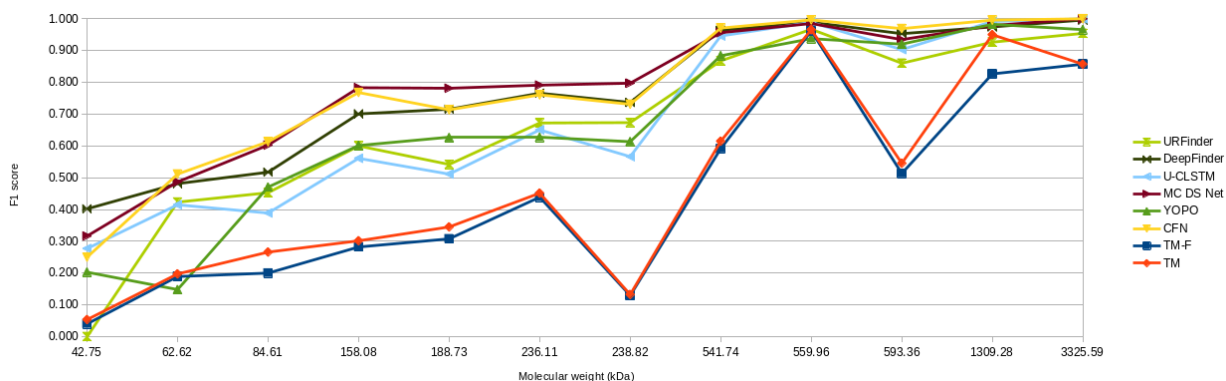


Figure 10: Method classification performance plot against particle molecular weight.

not taking into account “offline” training time. The success suggests that existing supervised models can do better than TM in practice, given the data is sufficiently realistic and/or model is robust to image acquisition parameter difference. Moreover, some unsupervised approaches Zeng et al. (2021); Zeng and Xu (2020) already show comparable or better performance on real datasets.

### Localization precision

Localizing exact center of a particle is important for accurate subtomogram averaging. During localization evaluation we have recorded average euclidean distance from predicted to ground truth particle center. CFN (Section 3.6) showed the best performance, closely followed by MC DS Net (Section 3.4) and YOPO (Section 3.5), again better than template matching almost on one full voxel (1nm). CFN and YOPO receive subtomograms as input and both use smart pooling approaches to maximize scale-invariance, allowing to accurately find bioparticles of different sizes. MC DS Net uses denoising that can remove noise around particles leading to improved localization precision.

### Neural network architectures

Four methods (DeepFinder, U-CLSTM, MC DS Net and partly URFinder) use advanced variations of U-Net Ronneberger et al. (2015) architecture, originally intended for accurate, voxel-level, biomedical semantic segmentation. CFN and YOPO do not rely on semantic segmentation rather work with subtomograms directly and do not require voxel level labels, making it more accessible for cryo-ET researchers.

### Performance correlates with molecular weight

Results (Table 6, Figure 10, Figure 11) show strong correlation between molecular weights and classification performance for all methods. All learning-based methods show consistent performance directly correlating with size, probably due to voxel count (volume) going down rapidly and not leaving enough voxels to be classified. At the same time, TM results have interesting difference, being able to distinguish some particles better than other. For example, TM

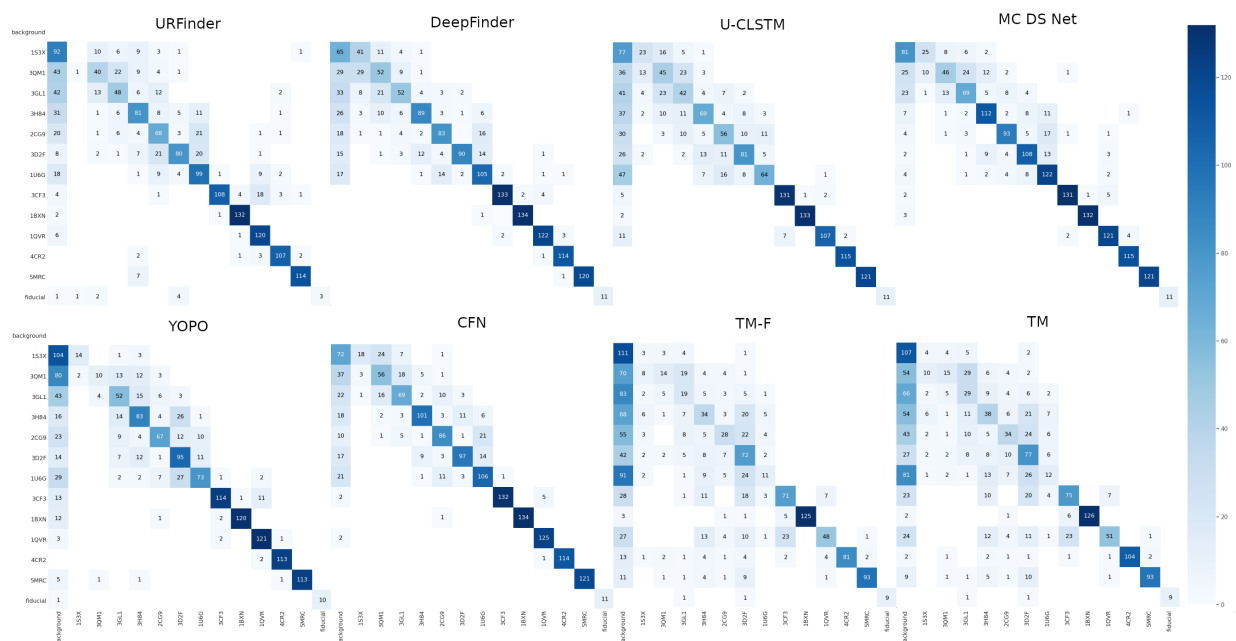


Figure 11: Classification confusion matrices of the compared methods. The particles are ordered by molecular weight. The colorbar indicates the number of correct classifications.

performs on-par with learning-based method with protein 1bxn (rubisco). Rubisco has high sphericity, large effective radius (Table 1) and four-fold symmetry, that fits well to template matching process. On the opposite, protein 1u6g is asymmetric, has average sphericity and effective radius, and is not distinguished well by TM.

## Future work

We strive to provide highly realistic dataset, and while the simulator shows good agreement with experimental data, it has not been quantitatively validated yet. We hope that in the next edition of the benchmark we can provide a fully annotated experimental tomogram as one of the test objectives.

## Acknowledgments

We want to thank all track participants for their contribution.

This work was supported by the European Research Council under the European Union's Horizon2020 Programme (ERC Consolidator Grant Agreement 724425 - BENDER) and the Nederlandse Organisatie voor Wetenschappelijke Onderzoek (Vici 724.016.001 and 741.018.201).

## References

- Tal Yahav, Tal Maimon, Einat Grossman, Idit Dahan, and Ohad Medalia. Cryo-electron tomography: gaining insight into cellular processes by structural approaches. *Current opinion in structural biology*, 21(5):670–677, 2011.
- Stefan Pfeffer and Julia Mahamid. Unravelling molecular complexity in structural cell biology. *Current opinion in structural biology*, 52:111–118, 2018.
- Achilleas S Frangakis, Jochen Böhm, Friedrich Förster, Stephan Nickell, Daniela Nicastro, Dieter Typke, Reiner Hegerl, and Wolfgang Baumeister. Identification of macromolecular complexes in cryoelectron tomograms of phantom cells. *Proceedings of the National Academy of Sciences*, 99(22):14153–14158, 2002.
- NR Voss, CK Yoshioka, M Radermacher, CS Potter, and B Carragher. Dog picker and tiltpicker: software tools to facilitate particle selection in single particle electron microscopy. *Journal of structural biology*, 166(2):205–213, 2009.

- Yuxiang Chen, Thomas Hrabe, Stefan Pfeffer, Olivier Pauly, Diana Mateus, Nassir Navab, and Friedrich Förster. Detection and identification of macromolecular complexes in cryo-electron tomograms using support vector machines. In *2012 9th IEEE International Symposium on Biomedical Imaging (ISBI)*, pages 1373–1376. IEEE, 2012.
- Philip R Baldwin, Yong Zi Tan, Edward T Eng, William J Rice, Alex J Noble, Carl J Negro, Michael A Cianfrocco, Clinton S Potter, and Bridget Carragher. Big data in cryoem: automated collection, processing and accessibility of em data. *Current opinion in microbiology*, 43:1–8, 2018.
- Feng Wang, Huichao Gong, Gaochao Liu, Meijing Li, Chuangye Yan, Tian Xia, Xueming Li, and Jianyang Zeng. Deeppicker: a deep learning approach for fully automated particle picking in cryo-em. *Journal of structural biology*, 195(3):325–336, 2016.
- Chengqian Che, Ruogu Lin, Xiangrui Zeng, Karim Elmaaroufi, John Galeotti, and Min Xu. Improved deep learning-based macromolecules structure classification from electron cryo-tomograms. *Machine vision and applications*, 29(8):1227–1236, 2018.
- Muyuan Chen, Wei Dai, Stella Y Sun, Darius Jonasch, Cynthia Y He, Michael F Schmid, Wah Chiu, and Steven J Ludtke. Convolutional neural networks for automated annotation of cellular cryo-electron tomograms. *Nature methods*, 14(10):983, 2017a.
- Ran Li, Xiangrui Zeng, Stephanie E Sigmund, Ruogu Lin, Bo Zhou, Chang Liu, Kaiwen Wang, Rui Jiang, Zachary Freyberg, Hairong Lv, et al. Automatic localization and identification of mitochondria in cellular electron cryo-tomography using faster-rcnn. *BMC bioinformatics*, 20(3):132, 2019.
- Ilja Gubins, Gijs van der Schot, Remco C. Veltkamp, Friedrich Förster, Xuefeng Du, Xiangrui Zeng, Zhenxi Zhu, Lufan Chang, Min Xu, Emmanuel Moebel, Antonio Martinez-Sanchez, Charles Kervrann, Tuan M. Lai, Xusi Han, Genki Terashi, Daisuke Kihara, Benjamin A. Himes, Xiaohua Wan, Jingrong Zhang, Shan Gao, Yu Hao, Zhilong Lv, Xiaohua Wan, Zhidong Yang, Zijun Ding, Xuefeng Cui, and Fa Zhang. Classification in Cryo-Electron Tomograms. In Silvia Biasotti, Guillaume Lavoué, and Remco Veltkamp, editors, *Eurographics Workshop on 3D Object Retrieval*. The Eurographics Association, 2019. ISBN 978-3-03868-077-2. doi:10.2312/3dor.20191061.
- Min Xu, Jitin Singla, Elitza I Tocheva, Yi-Wei Chang, Raymond C Stevens, Grant J Jensen, and Frank Alber. De novo structural pattern mining in cellular electron cryotomograms. *Structure*, 27(4):679–691, 2019.
- Min Xu and Frank Alber. Automated target segmentation and real space fast alignment methods for high-throughput classification and averaging of crowded cryo-electron subtomograms. *Bioinformatics*, 29(13):i274–i282, 2013.
- Xiangrui Zeng and Min Xu. Gum-net: Unsupervised geometric matching for fast and accurate 3d subtomogram image alignment and averaging. In *Proceedings of the IEEE/CVF Conference on Computer Vision and Pattern Recognition*, pages 4073–4084, 2020.
- Hans Rullgård, L-G Öfverstedt, Sergey Masich, Bertil Daneholt, and Ozan Öktem. Simulation of transmission electron microscope images of biological specimens. *Journal of microscopy*, 243(3):234–256, 2011.
- RDB Fraser, TP MacRae, and E Suzuki. An improved method for calculating the contribution of solvent to the x-ray diffraction pattern of biological molecules. *Journal of Applied Crystallography*, 11(6):693–694, 1978.
- Miloš Vulović, Raimond BG Ravelli, Lucas J van Vliet, Abraham J Koster, Ivan Lazić, Uwe Lücken, Hans Rullgård, Ozan Öktem, and Bernd Rieger. Image formation modeling in cryo-electron microscopy. *Journal of structural biology*, 183(1):19–32, 2013.
- Daniel Ruijters and Philippe Thévenaz. Gpu prefilter for accurate cubic b-spline interpolation. *The Computer Journal*, 55(1):15–20, 2012.
- Ilja Gubins, Marten L Chaillet, Gijs van der Schot, Remco C Veltkamp, Friedrich Förster, Yu Hao, Xiaohua Wan, Xuefeng Cui, Fa Zhang, Emmanuel Moebel, et al. Shrec 2020: Classification in cryo-electron tomograms. *Computers & Graphics*, 91:279–289, 2020.
- Huimin Huang, Lanfen Lin, Ruofeng Tong, Hongjie Hu, Qiaowei Zhang, Yutaro Iwamoto, Xianhua Han, Yen-Wei Chen, and Jian Wu. Unet 3+: A full-scale connected unet for medical image segmentation. In *ICASSP 2020-2020 IEEE International Conference on Acoustics, Speech and Signal Processing (ICASSP)*, pages 1055–1059. IEEE, 2020.
- Kaiming He, Xiangyu Zhang, Shaoqing Ren, and Jian Sun. Deep residual learning for image recognition. In *Proceedings of the IEEE conference on computer vision and pattern recognition*, pages 770–778, 2016a.
- Kensho Hara, Hirokatsu Kataoka, and Yutaka Satoh. Learning spatio-temporal features with 3d residual networks for action recognition. In *Proceedings of the IEEE International Conference on Computer Vision Workshops*, pages 3154–3160, 2017.

- Zongwei Zhou, Md Mahfuzur Rahman Siddiquee, Nima Tajbakhsh, and Jianming Liang. Unet++: A nested u-net architecture for medical image segmentation. In *Deep learning in medical image analysis and multimodal learning for clinical decision support*, pages 3–11. Springer, 2018.
- Diederik P Kingma and Jimmy Ba. Adam: A method for stochastic optimization. *arXiv preprint arXiv:1412.6980*, 2014.
- Ilya Loshchilov and Frank Hutter. Sgdr: Stochastic gradient descent with warm restarts. *arXiv preprint arXiv:1608.03983*, 2016.
- Emmanuel Moebel, Antonio Martinez-Sanchez, Damien Lariviere, Eric Fourmentin, Julio Ortiz, Wolfgang Baumeister, and Charles Kervrann. Deep learning improves macromolecules localization and identification in 3d cellular cryo-electron tomograms. *bioRxiv*, 2020.
- Carole H Sudre, Wenqi Li, Tom Vercauteren, Sebastien Ourselin, and M Jorge Cardoso. Generalised dice overlap as a deep learning loss function for highly unbalanced segmentations. In *Deep learning in medical image analysis and multimodal learning for clinical decision support*, pages 240–248. Springer, 2017.
- Olaf Ronneberger, Philipp Fischer, and Thomas Brox. U-net: Convolutional networks for biomedical image segmentation. In *International Conference on Medical image computing and computer-assisted intervention*, pages 234–241. Springer, 2015.
- Kai Zhang, Wangmeng Zuo, Yunjin Chen, Deyu Meng, and Lei Zhang. Beyond a gaussian denoiser: Residual learning of deep cnn for image denoising. *IEEE transactions on image processing*, 26(7):3142–3155, 2017.
- Fausto Milletari, Nicola Rieke, Maximilian Baust, Marco Esposito, and Nassir Navab. Cfcn: segmentation via coarse to fine context memory. In *International Conference on Medical Image Computing and Computer-Assisted Intervention*, pages 667–674. Springer, 2018.
- Xingjian Shi, Zhouong Chen, Hao Wang, Dit-Yan Yeung, Wai-Kin Wong, and Wang-chun Woo. Convolutional lstm network: A machine learning approach for precipitation nowcasting. *arXiv preprint arXiv:1506.04214*, 2015.
- Liang-Chieh Chen, George Papandreou, Iasonas Kokkinos, Kevin Murphy, and Alan L Yuille. Deeplab: Semantic image segmentation with deep convolutional nets, atrous convolution, and fully connected crfs. *IEEE transactions on pattern analysis and machine intelligence*, 40(4):834–848, 2017b.
- Nguyen Phuoc Nguyen, Ilker Ersoy, Jacob Gotberg, Filiz Bunyak, and Tommi A White. Drpnet: automated particle picking in cryo-electron micrographs using deep regression. *BMC bioinformatics*, 22(1):1–28, 2021.
- Ilja Gubins and Remco C Veltkamp. Deeply cascaded u-net for multi-task image processing. *arXiv preprint arXiv:2005.00225*, 2020.
- Xiangrui Zeng, Anson Kahng, Liang Xue, Julia Mahamid, Yi-Wei Chang, and Min Xu. Disca: high-throughput cryo-et structural pattern mining by deep unsupervised clustering. *bioRxiv*, 2021.
- Kaiming He, Xiangyu Zhang, Shaoqing Ren, and Jian Sun. Identity mappings in deep residual networks. In *European conference on computer vision*, pages 630–645. Springer, 2016b.
- Fisher Yu and Vladlen Koltun. Multi-scale context aggregation by dilated convolutions. *arXiv preprint arXiv:1511.07122*, 2015.
- Tsung-Yi Lin, Priya Goyal, Ross Girshick, Kaiming He, and Piotr Dollár. Focal loss for dense object detection. In *Proceedings of the IEEE international conference on computer vision*, pages 2980–2988, 2017.
- Thomas Hrabe, Yuxiang Chen, Stefan Pfeffer, Luis Kuhn Cuellar, Ann-Victoria Mangold, and Friedrich Förster. Pytom: a python-based toolbox for localization of macromolecules in cryo-electron tomograms and subtomogram analysis. *Journal of structural biology*, 178(2):177–188, 2012.